




## Chiral droplets and current-driven motion in ferromagnets

Naveen Sisodia <sup>1</sup>, Pranaba Kishor Muduli <sup>1</sup>, Nikos Papanicolaou,<sup>2</sup> and Stavros Komineas <sup>3</sup>

<sup>1</sup>Department of Physics, Indian Institute of Technology Delhi, Hauz Khas, New Delhi 110016, India

<sup>2</sup>Department of Physics, University of Crete, 70013 Heraklion, Crete, Greece

<sup>3</sup>Department of Mathematics and Applied Mathematics, University of Crete, 70013 Heraklion, Crete, Greece



(Received 3 September 2020; revised 18 November 2020; accepted 4 January 2021; published 19 January 2021)

We find numerically skyrmionic textures with skyrmion number  $Q = 0$  in ferromagnets with the Dzyaloshinskii-Moriya interaction, perpendicular anisotropy, and the magnetostatic field. These have a skyrmion part and an antiskyrmion part, and they may be called chiral droplets. They are stable in an infinite film as well as in disk-shaped magnetic elements. Droplets are found in films for values of the parameters close to the transition from the ferromagnetic to the spiral phase. Under spin-transfer torque, they move in the direction of the spin flow and behave as solitary waves of Newtonian character, in stark contrast to the Hall dynamics of the standard  $Q = 1$  skyrmion.

DOI: [10.1103/PhysRevB.103.024431](https://doi.org/10.1103/PhysRevB.103.024431)

### I. INTRODUCTION

Since the experimental observation of skyrmions in ferromagnetic materials with the Dzyaloshinskii-Moriya (DM) interaction, a substantial amount of work has been devoted to their statics and dynamics [1]. Chiral skyrmions are topological solitons that have the same topological features as magnetic bubbles [2], but the detailed features of the chiral skyrmion profile are specific to it [3,4]. Most work has largely focused on the axially symmetric chiral skyrmion predicted in Refs. [3,5]. Different crystal symmetries give rise to various types of DM interactions, and these, in turn, define the kinds of skyrmions that can be stabilized [5,6]. In Ref. [7] the observation of antiskyrmions was reported, that is, skyrmions that have a winding number opposite to that of the standard axially symmetric skyrmions.

The dynamics of skyrmions is linked to their topology [8,9]; specifically, it depends on the topological number, usually called the skyrmion number  $Q$ . Skyrmions with  $Q \neq 0$ , such as the axially symmetric skyrmions or the antiskyrmions with  $Q = \pm 1$ , are called *topological*, while skyrmionic textures with  $Q = 0$  are called *topologically trivial*. Topological,  $Q \neq 0$ , skyrmions are spontaneously pinned in a ferromagnetic film [9,10]. By contrast, topologically trivial magnetic solitons propagate freely as Newtonian particles. An example is provided by the skyrmionium [8,11,12], an axially symmetric skyrmionic texture with trivial topology.

We focus on  $Q = 0$  solitons that can be constructed as skyrmion-antiskyrmion pairs. In Refs. [13,14], observations of topologically trivial objects in DM materials were reported, with a skyrmion part and an antiskyrmion part in the case of Ref. [14]. In Ref. [15],  $Q = 0$  textures were found numerically within a model with frustrated isotropic exchange and DM interaction, and they are termed “chimera skyrmions” due to the coexistence of skyrmion and antiskyrmion parts.

We find numerically, within a model with DM interaction and the magnetostatic field, a skyrmionic texture with  $Q = 0$

that has a skyrmion part and an antiskyrmion part. This is an asymmetric configuration, and its shape resembles that of a liquid droplet. The skyrmion part occupies a much larger area than the antiskyrmion part. In a recent work [16], the droplet was found to be stable without the magnetostatic field contribution. We find that a static droplet is a stable structure in a ferromagnetic infinite film as well as in a disk-shaped element, within appropriate ranges of the model parameters. In the case of a film, we study the dynamics of the chiral droplet under in-plane current. The droplet is traveling in the direction of the current and presents Newtonian dynamics and no Magnus force effect.

The outline of the paper is as follows. Section II defines the model and the notations used in the paper. Section III presents the static solutions for chiral droplets in an infinite film. Section IV studies the dynamical behavior of a droplet under current. Section V presents droplet solutions in a disk-shaped particle. Section VI contains our concluding remarks. In the Appendix we give a brief explanation of the skyrmion and antiskyrmion configuration represented via the stereographic variable.

### II. FORMULATION

We consider a ferromagnetic film with exchange, easy-axis anisotropy perpendicular to the film and interfacial DM interaction. We denote the saturation magnetization by  $M_s$  and the normalized magnetization vector by  $\mathbf{m} = (m_x, m_y, m_z)$ , with  $m^2 = 1$ . The magnetic energy is

$$\begin{aligned}
 E = & A \int [(\partial_x \mathbf{m})^2 + (\partial_y \mathbf{m})^2] dV + K \int (1 - m_z^2) dV \\
 & + D \int [\hat{\mathbf{e}}_x \cdot (\partial_y \mathbf{m} \times \mathbf{m}) - \hat{\mathbf{e}}_y \cdot (\partial_x \mathbf{m} \times \mathbf{m})] dV \\
 & - \frac{1}{2} \mu_0 M_s^2 \int \mathbf{h}_m \cdot \mathbf{m} dV, \quad (1)
 \end{aligned}$$

where  $\hat{e}_x, \hat{e}_y, \hat{e}_z$  denote the unit vectors in the respective directions,  $A$  is the exchange parameter,  $K$  is the easy-axis anisotropy parameter,  $D$  is the DM parameter, and  $\mathbf{h}_m$  is the magnetostatic field normalized to the saturation magnetization.

Considering the thin-film approximation for the magnetostatic field, we decompose it into a local part,  $-m_z \hat{e}_z$ , and a nonlocal part,  $\mathbf{h}'_m$ ,

$$\mathbf{h}_m = -m_z \hat{e}_z + \mathbf{h}'_m, \quad (2)$$

and note that  $\mathbf{h}'_m$  tends to zero for very thin films. Substituting Eq. (2) in Eq. (1) gives rise to an effective anisotropy parameter (that includes the local part of the magnetostatic field)

$$K_{\text{eff}} = K - \frac{1}{2} \mu_0 M_s^2. \quad (3)$$

The statics and dynamics of the magnetization vector are described by the Landau-Lifshitz equation derived from the energy in Eq. (1). Including a Gilbert damping term, we have

$$\partial_t \mathbf{m} = -\gamma \mathbf{m} \times \mathbf{H}_{\text{eff}} + \alpha \mathbf{m} \times \partial_t \mathbf{m}, \quad (4)$$

where  $\alpha$  is the damping parameter. The effective field is defined by

$$\mathbf{H}_{\text{eff}} = -\frac{1}{M_s} \frac{\delta E}{\delta \mathbf{m}}, \quad (5)$$

and it has the form

$$\begin{aligned} \mathbf{H}_{\text{eff}} = \mu_0 M_s \left[ \frac{2A}{\mu_0 M_s^2} \Delta \mathbf{m} + \frac{2K_{\text{eff}}}{\mu_0 M_s^2} m_z \hat{e}_z \right. \\ \left. + \frac{2D}{\mu_0 M_s^2} (\hat{e}_y \times \partial_x \mathbf{m} - \hat{e}_x \times \partial_y \mathbf{m}) + \mathbf{h}'_m \right]. \quad (6) \end{aligned}$$

It is instructive to write the dimensionless form of Eq. (4). Using  $\ell_w = \sqrt{A/K_{\text{eff}}}$  as the unit of length, we obtain the dimensionless Landau-Lifshitz-Gilbert (LLG) equation

$$\partial_\tau \mathbf{m} = -\mathbf{m} \times \mathbf{h}_{\text{eff}} + \alpha \mathbf{m} \times \partial_\tau \mathbf{m}, \quad (7)$$

where

$$\mathbf{h}_{\text{eff}} = \Delta \mathbf{m} + m_z \hat{e}_z + 2\epsilon (\hat{e}_y \times \partial_x \mathbf{m} - \hat{e}_x \times \partial_y \mathbf{m}) + \frac{\mathbf{h}'_m}{\kappa}, \quad (8)$$

and we have introduced the dimensionless DM parameter

$$\epsilon = \frac{D}{2\sqrt{AK_{\text{eff}}}} \quad (9)$$

and the dimensionless anisotropy parameter

$$\kappa = \frac{2K_{\text{eff}}}{\mu_0 M_s^2}. \quad (10)$$

Equation (8) indicates that varying  $\kappa$  amounts to tuning the effect of the magnetostatic field. The normalized time variable in Eq. (7) is

$$\tau = \frac{t}{\tau_0}, \quad \tau_0 = \frac{1}{\gamma \mu_0 M_s \kappa}. \quad (11)$$

When we set  $\mathbf{h}'_m = 0$  in model (8), the ground state is the spiral for  $\epsilon > 2/\pi \approx 0.637$ , while we have the ferromagnetic state for  $\epsilon < 2/\pi$  [3]. Only the latter regime is considered in this work. Skyrmions with axial symmetry are stable excited

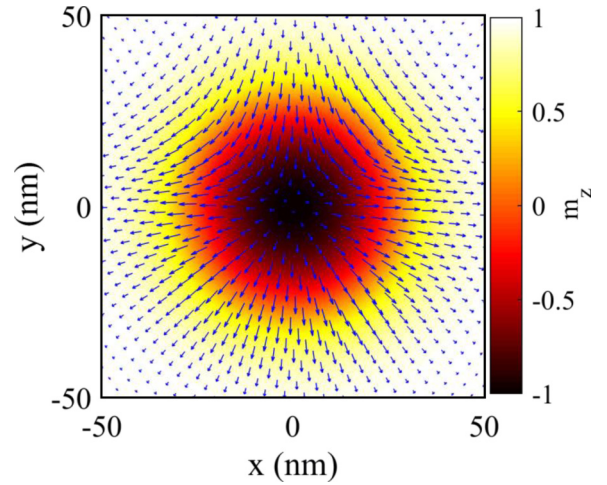


FIG. 1. The magnetization configuration produced by the form (13) representing a skyrmion-antiskyrmion pair. The lower half of this configuration has the features of a skyrmion, and the upper half has the features of an antiskyrmion. This is used as the initial condition in the energy relaxation algorithm for finding a static solution of the equation.

states on the ferromagnetic state. All magnetic configurations are characterized by the skyrmion number defined as

$$Q = \frac{1}{4\pi} \int q \, dx \, dy, \quad q = \mathbf{m} \cdot (\partial_y \mathbf{m} \times \partial_x \mathbf{m}), \quad (12)$$

where  $q$  is the *topological density*. The skyrmion number  $Q$  is integer valued for all magnetic configurations with a constant  $\mathbf{m}$  at spatial infinity. For definiteness, we assume  $\mathbf{m} = (0, 0, 1)$  at spatial infinity in all our calculations.

### III. CHIRAL DROPLET TEXTURES

We are looking for solutions of model (7) with skyrmion number  $Q = 0$ . An ansatz for a  $Q = 0$  configuration is conveniently given in terms of the stereographic variable, defined in the Appendix, as

$$\Omega_0 = \frac{a}{x + i|y|}, \quad (13)$$

where  $a$  is an arbitrary constant. The magnetization configuration produced by the form (13) is shown in Fig. 1. Half of this configuration has the features of a skyrmion similar to the form (A2), and the other half has the features of an antiskyrmion similar to the form (A3). Such a configuration may be called a *skyrmion-antiskyrmion* pair.

We perform numerical simulations using MUMAX3 [17]. We use the form (13) as the initial condition and apply an energy minimization procedure. First, we use the minimize() function of MUMAX3 that applies a conjugate gradient method for energy minimization. The energy is minimized until the error in the magnetization is smaller than  $10^{-5}$  in every micromagnetic cell. We then integrate the Landau-Lifshitz-Gilbert equation without the precession term until either the total energy of the system reaches the numerical noise floor of the simulation or the total simulation time exceeds 10 ns. The above methodology converges to a static skyrmion-antiskyrmion configuration for a narrow range of

TABLE I. Values for material parameters used in most of our simulations presented in the figures:  $M_s$  is the saturation magnetization,  $A$  is the exchange parameter,  $K$  is the easy-axis anisotropy parameter [ $K_{\text{eff}}$  includes the local effect of the magnetostatic interaction according to Eq. (3)], and  $D$  is the DM parameter.

Parameter	Value
$M_s$	$8.38 \times 10^5$ A/m
$A$	$1.1 \times 10^{-11}$ J/m
$K$ ( $K_{\text{eff}}$ )	$11.93$ ( $7.518$ ) $\times 10^5$ J/m <sup>3</sup>
$D$	$3.5 \times 10^{-3}$ J/m <sup>2</sup>

values of the dimensionless parameters  $\epsilon$ ,  $\kappa$  and for a range of film thicknesses.

The complicated numerical minimization protocol followed is necessary because we found that a simple minimization via the micromagnetics package MUMAX3 can give spurious static configurations of the form studied in this work.

In most of the numerical simulations presented in the following figures, we use the set of parameter values shown in Table I. The resulting values for the length scale and timescale in Eq. (7) are  $\ell_w = 3.81$  nm and  $\tau_0 = 5.14$  ps, respectively. The values of the dimensionless parameters are

$$\epsilon = 0.6086, \quad \kappa = 1.704. \quad (14)$$

Figure 2 shows a skyrmion-antiskyrmion configuration which is found as a static solution of the LLG equation (4). This resembles, in its overall shape, a droplet of liquid, and we will therefore refer to it as a *chiral droplet* (or, simply, a droplet). A larger part of the configuration has the features of a skyrmion, and a smaller part has the features of an antiskyrmion. It is not axially symmetric, nor does it have a circular shape. In the example shown in Fig. 2, the antiskyrmion part is at the top part of the droplet, but the configuration can be rotated without changing its energy.

Figure 3 shows the distribution of the topological density  $q$  defined in Eq. (12) for the skyrmion in Fig. 2. The area of negative topological density is concentrated in the small part of the droplet where the antiskyrmion is located, and it takes very high values. The area of positive  $q$  is spread over a much larger area around the droplet domain wall, and it takes smaller values.

We could find stable chiral droplets only in thin films. For  $d_f = 0.5$  nm, we find a static droplet for values of the dimensionless parameter in a narrow range around  $\epsilon = 0.61$ . Keeping  $\epsilon$  constant, we could choose the DM parameter in the range  $2.9 \text{ mJ/m}^2 \leq D \leq 6 \text{ mJ/m}^2$  (while varying the anisotropy parameter  $K$  appropriately). We could also find stable droplets for film thickness smaller than  $d_f = 0.5$  nm and for similar parameter values. Also, a stable droplet for film thickness  $d_f = 1$  nm for the parameter values  $D = 6 \text{ mJ/m}^2$ ,  $K = 26.5 \times 10^5 \text{ J/m}^2$  (other parameters are as in Table I). These values correspond to  $\epsilon = 0.6086$ ,  $\kappa = 5.01$ . The droplet is stable for a range of parameter values around the ones given above. We finally note that, as the parameter space is large and hard to explore exhaustively, we cannot exclude that the droplet may also exist for values of the parameters beyond those reported in this paper.

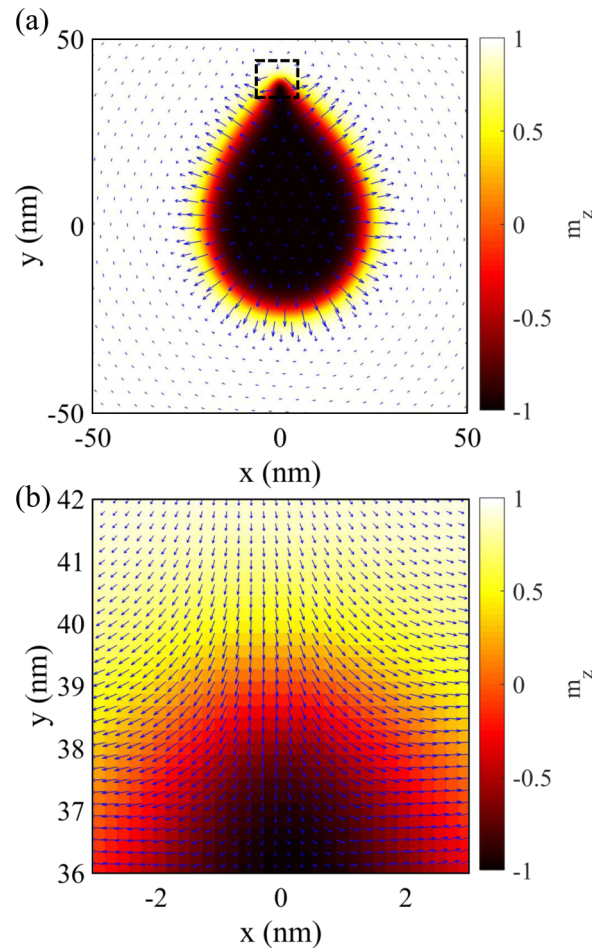


FIG. 2. (a) A static skyrmion-antiskyrmion droplet with  $Q = 0$  found numerically for the parameter values given in Table I and for film thickness  $d_f = 0.5$  nm. For comparison, a  $Q = 1$  skyrmion in the same system has a radius of  $\sim 16$  nm. (b) Blowup of the antiskyrmion part of the configuration, where we show the full resolution of the simulation. The simulated domain in the plane of the film is  $400 \times 400 \text{ nm}^2$ , and periodic boundary conditions are used. The cell size in the simulations is approximately  $0.195 \times 0.195 \times 0.5 \text{ nm}^3$  ( $2048 \times 2048 \times 1$  cells). We have performed simulations with different cell sizes to confirm that the presented droplet configuration does not depend on the cell size.

In order to understand the droplet configuration, we have to consider two main factors. We first note that the DM energy gives a negative contribution only for the skyrmion part. This is thus expanded at the expense of the antiskyrmion part, which is suppressed. In the next step, we consider only the domain wall region and note that the exchange energy increases as the antiskyrmion part is suppressed and more rapid changes of the magnetization occur. The result of the two competing mechanisms is a small antiskyrmion part that protrudes out of the rest of the domain wall in order to allow more space for the domain wall of the skyrmion part. Implicit in the above arguments is the assumption that the skyrmion radius is similar to the case of the axially symmetric skyrmion and it can be considered a given parameter.

The axially symmetric skyrmion is stabilized by the DM interaction, and its size depends on the DM interaction



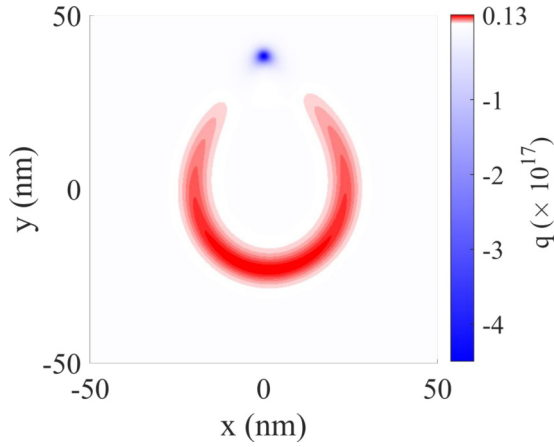


FIG. 3. The topological density  $q$  for the chiral droplet in Fig. 2. The part where  $q < 0$  (blue) occupies a very small region compared to the part where  $q > 0$  (red). The density  $q$  takes very large negative values in a small region, while in the region with positive values,  $q$  is small. The integrated topological density, or  $Q$ , is zero.

strength. For the parameters in Table I, its diameter is numerically found to be approximately 40 nm, and it is thus comparable to the size of the droplet. This shows that the DM interaction is responsible for the stabilization of the droplet, too. This is further verified by the fact that the droplets are not stable when we continuously vary  $D$  to zero. The above show that the chiral droplets are distinct from other topologically trivial textures studied before, such as magnetic bubbles with a zero topological number.

We conclude this section with a reference to previous works on related textures. Reference [16] reports that the chiral droplet is stable for  $2/\pi \approx 0.63 > \epsilon > 0.59$ , within an extended study on the diversity of chiral skyrmionic textures in a model without magnetostatic field. Textures with skyrmion and antiskyrmion parts (“chimera skyrmions”), similar to the ones reported here, have been found numerically and studied within a model with frustrated isotropic exchange interaction and DM interaction [15,18,19]. Related to our droplet are also the  $Q = 0$  magnetic bubbles discussed within the relevant literature [2] and, more recently, numerically calculated [20]. The latter are not chiral; they are stabilized primarily by the magnetostatic interaction (and a bias field), and their overall shape is almost circular. Another related structure (also termed a droplet) was reported in Refs. [21,22], in films without DM interaction, and it is a dynamical configuration exhibiting precession of spins. In the chiral droplet studied here, spin precession does not occur due to the breaking of rotational symmetry in the magnetization space introduced by the chiral interaction. In Ref. [23], Skyrmion-antiskyrmion pairs were studied for a model with only exchange interaction, and they were found to be necessarily propagating. A notable difference between the last two studies of topologically trivial textures and the present droplet is that the latter is found to be a static configuration.

#### IV. MOTION UNDER SPIN-TRANSFER TORQUE

We probe the dynamics of the  $Q = 0$  droplet by applying an in-plane charge current flowing in the magnetic film. We

model this system via the LLG equation including a Zhang-Li spin-transfer torque term [24]

$$(\partial_t + U_\mu \partial_\mu) \mathbf{m} = -\gamma \mathbf{m} \times \mathbf{H}_{\text{eff}} + \mathbf{m} \times (\alpha \partial_t + \beta U_\mu \partial_\mu) \mathbf{m}, \quad (15)$$

where we have used the notation  $x_\mu$  with  $\mu = 1$  or  $2$  for the two coordinates in the film plane. The velocity of the electron flow is  $(U_1, U_2)$ , and we will consider the two cases  $(U_1, U_2) = (U, 0)$  and  $(U_1, U_2) = (0, U)$ , i.e., a current flowing in the  $x$  direction and in the  $y$  direction, respectively. The flow velocity  $U$  is called the adiabatic spin torque parameter, and it is given by

$$U = \frac{Pg\mu_B}{2|e|M_s} J_e, \quad (16)$$

where  $J_e$  is the current density,  $P$  is the degree of polarization,  $\mu_B$  is the Bohr magneton, and  $g = 2$  is the gyromagnetic ratio. The parameter  $\beta$ , called the degree of adiabaticity, represents the contribution of the nonadiabatic spin torque term relative to the adiabatic one.

If we assume rigid translational motion of the droplet with a velocity  $\mathbf{V} = (V_1, V_2)$ , i.e., we make the traveling wave ansatz, then we have  $\partial_t \mathbf{m} = -V_\nu \partial_\nu \mathbf{m}$ . We substitute this in Eq. (15), and following the method of Thiele [25], we take the cross product of both sides with  $\partial_\lambda \mathbf{m}$ , then contract with  $\mathbf{m}$ , integrate the resulting equations for  $\lambda = 1, 2$  over all space, and set  $Q = 0$  [26]. This shows that the motion is in the direction of the current flow with velocity [26,27]

$$\mathbf{V} = \frac{\beta}{\alpha} \mathbf{U}. \quad (17)$$

Therefore, in a steady-state motion, the droplet is not expected to exhibit a component of the motion perpendicular to the current, in contrast to the typical dynamics of the  $Q = 1$  skyrmion.

For a more detailed description of the droplet motion and of the following simulations, we recall a fundamental result given in Ref. [26]. That is, a propagating solution of Eq. (15) with velocity  $V$  is also a solitary wave solution of the conservative Landau-Lifshitz equation, i.e., Eq. (4) with  $\alpha = 0$ , albeit with a different velocity  $V_{\text{LL}}$ . Specifically, let us assume an electron flow velocity  $(U, 0)$  and a droplet propagating with velocity  $V$  in the direction of the current, i.e.,  $\mathbf{m} = \mathbf{m}(x - Vt, y)$ . Equation (15) gives

$$(U - V) \partial_x \mathbf{m} = -\gamma \mathbf{m} \times \mathbf{H}_{\text{eff}} + \alpha \left( \frac{\beta}{\alpha} U - V \right) \mathbf{m} \times \partial_x \mathbf{m}. \quad (18)$$

If we assume a propagating solution of Eq. (18) with velocity  $V = \frac{\beta}{\alpha} U$ , then the same configuration is a solitary wave satisfying the conservative ( $\alpha = 0$ ) Landau-Lifshitz equation (4) with a velocity

$$V_{\text{LL}} = V - U = \left( \frac{\beta}{\alpha} - 1 \right) U. \quad (19)$$

In the special case  $\beta = \alpha$ , a static solution of Eq. (4), say,  $\mathbf{m}_0(x, y)$ , gives the propagating solution  $\mathbf{m}(x, y, t) = \mathbf{m}_0(x - Ut, y)$  of Eq. (18), with velocity  $V = U$ .

We now proceed to numerical simulations in which we use as the initial condition the static droplet shown in Fig. 2.

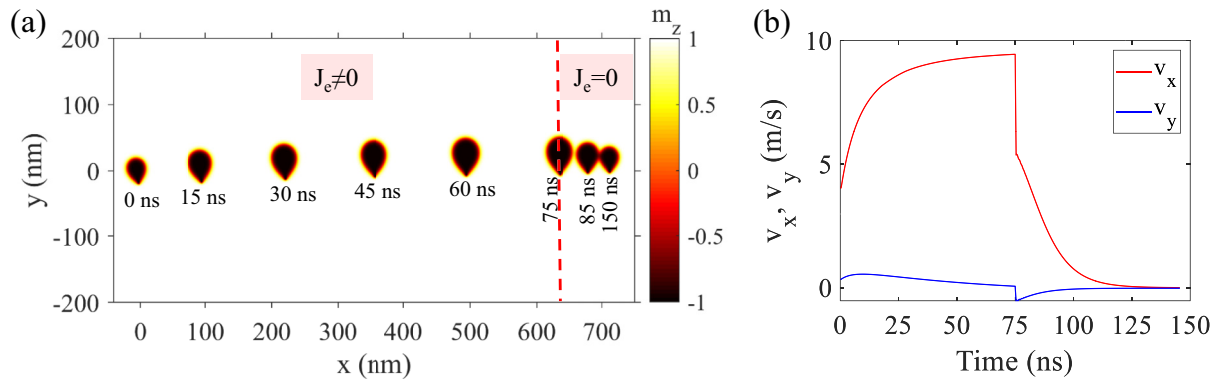


FIG. 4. (a) Snapshots of an initially static droplet during a simulation where a current  $J_e$  is applied in the  $x$  direction for times  $0 \leq t \leq 75$  ns. The parameters are  $U = 3.86$  m/s,  $\beta = 0.075$ , and the damping parameter is  $\alpha = 0.03$ . (b) The velocity of the droplet as a function of time. Upon switching on the current the velocity is  $V = 4.02$  m/s in the current direction (denoted  $V_x$ ). The droplet is then accelerated up to  $V = 9.45$  m/s, which is close to the value  $2.5U$ . After switching off the current, the velocity drops instantly by approximately 4 m/s (which is close to  $U$ ), to  $V = 5.37$  m/s. The droplet continues to travel, and the damping term decelerates the motion until it stops. The component of the velocity perpendicular to the current (denoted  $V_y$ ) is very small and goes to zero for steady-state motion.

For the results presented in this section, we use a domain of  $400 \times 400$  nm<sup>2</sup> with periodic boundary conditions. The cells have dimensions of approximately  $0.39 \times 0.39 \times 0.5$  nm<sup>3</sup> ( $1024 \times 1024 \times 1$  cells); that is, the lattice is coarser than the one used for the achievement of the static droplet in Fig. 2. We use  $P = 0.56$ , and for our typical choice of current  $J_e = 1.0 \times 10^{11}$  A/m<sup>2</sup>, we have a flow velocity  $U = 3.86$  m/s.

To follow the dynamics of the droplet, we measure its position  $(X, Y)$  using the formulas

$$X = \frac{\int x(m_z - 1) dx dy}{\int (m_z - 1) dx dy}, \quad Y = \frac{\int y(m_z - 1) dx dy}{\int (m_z - 1) dx dy}. \quad (20)$$

We calculate the skyrmion velocity using finite differences of the position.

In the following simulations, we have chosen a current in the  $x$  direction and a damping parameter  $\alpha = 0.03$ . We use as the initial condition the droplet  $\mathbf{m}_0(x, y)$  in Fig. 2 rotated by  $\pi$  (the reason for the rotation will become apparent in the following). For  $\beta = \alpha$  we observe that the droplet of the initial condition is traveling with velocity  $V = U$  (within numerical error) in the direction of the current,  $\mathbf{m} = \mathbf{m}_0(x - Ut, y)$ , as anticipated from the discussion in connection with Eq. (19). During the simulation the initial droplet remains unchanged. We also observe a small component of the velocity  $\sim 0.15$  m/s perpendicular to the current direction, and we attribute it to numerical errors.

In the next simulation, we choose  $\beta = 0.075$  (that is,  $\beta = 2.5\alpha$ ). A current is applied for the time interval  $0 \leq t \leq 75$  ns, and it is then switched off. Figure 4 shows snapshots of the droplet during the simulation and the velocity of the droplet as a function of time. Upon switching on the current the droplet instantly acquires a velocity  $V$  in the current direction, which is close to  $U$ . It is subsequently accelerated up to  $V = 9.45$  m/s, which is close to the value  $2.5U$  and seems to saturate. The propagating droplet is different (larger) than the static one, as clearly seen in the snapshots.

When the current is switched off, at  $t = 75$  ns the droplet velocity is reduced instantly by approximately 4 m/s (which is

close to  $U$ ) to  $V = 5.37$  m/s. From this point on, the relevant equation is Eq. (4), while the reduction of the velocity is anticipated based on Eq. (19).

Let us summarize the procedure. The electron flow [second term on the left in Eq. (15)] induces an initial jump in the droplet velocity. Further than that, the current initially *accelerates* the droplet, which thus presents Newtonian dynamics. Note that this is analogous to the case of a skyrmionium [26]. The configuration gradually converges to a solitary wave solution of the conservative Landau-Lifshitz equation (see [28] for a proof of this procedure in a similar problem). The solitary wave continues to travel also after the current is switched off. The damping term decelerates the motion until it eventually stops. We measure a small component of the velocity in the direction perpendicular to the current ( $V_y$ ) during the acceleration and the deceleration phase. Part of it is due to the way we measure the position of the droplet, and another part is due to numerical errors. Specifically, the droplet grows in size as it accelerates and shrinks as it decelerates, causing its center, as we define it, to shift in the vertical direction. It cannot be excluded that part of the vertical shift is a genuine physical phenomenon. However, given the accuracy of the present numerical calculation, this cannot be claimed on the basis of the reported results.

In the next simulations, we use as the initial condition the droplet exactly as shown in Fig. 2. We choose  $\alpha = 0.1$  and  $\beta = 0.2$ . The larger damping is chosen in order to avoid transients and obtain the essential dynamics in a shorter simulation time. Furthermore, we now choose  $P = 0.538$ , and this gives  $U = 3.72$  m/s.

We apply a current in the  $x$  direction, or  $(U_1, U_2) = (U, 0)$ . Figure 5(a) shows snapshots of the droplet during the simulation. The motion is initially complicated, with the droplet making a full  $\pi$  turn. For times greater than 150 ns steady-state motion is reached, and the velocity has a constant value of 7.41 m/s along the direction of the current, in very good agreement with the theoretical prediction  $V = 2U$  given in Eq. (17). We finally mention that for large values of  $\beta$  (e.g.,  $\beta = 5\alpha$ ) the droplet is destroyed while it is moving, by

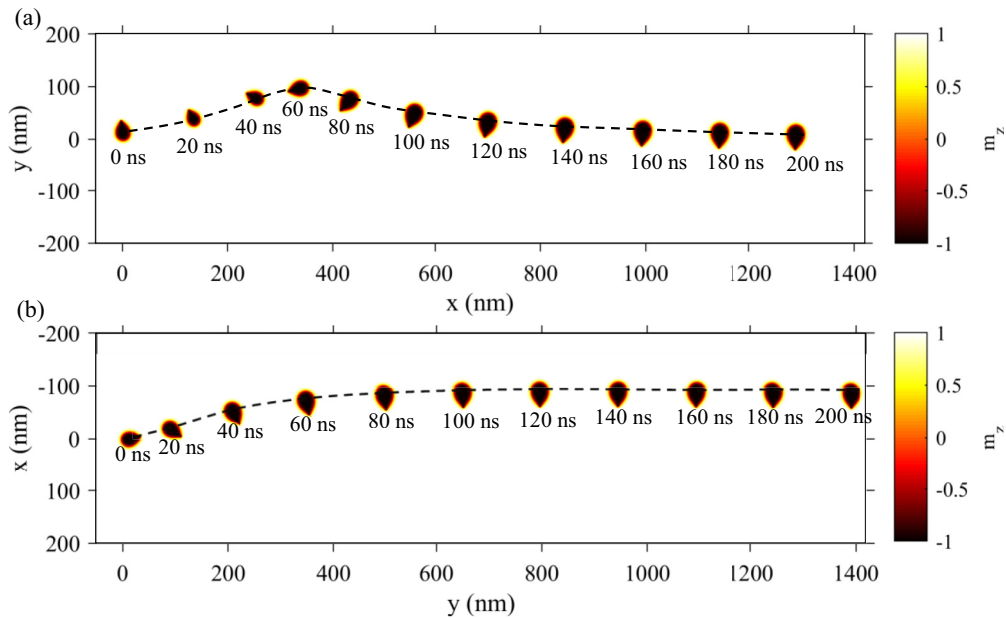


FIG. 5. Snapshots of the droplet in Fig. 2 when it is placed under spin torque at time  $t = 0$  and is set in motion. The flow velocity is (a)  $(U, 0)$  and (b)  $(0, U)$  with  $U = 3.72$  m/s. The damping parameter is  $\alpha = 0.1$ , and the nonadiabaticity parameter is  $\beta = 0.2$ . The simulation domain is  $400 \times 400$  nm<sup>2</sup>, and we apply periodic boundary conditions.

expanding in size. We continue to present the full set of our simulations before we proceed to give an explanation for the steady state achieved by the droplet.

In the next simulation, we choose a current along the  $y$  direction, or  $(U_1, U_2) = (0, U)$ . Figure 5(b) shows a series of snapshots of the droplet during the motion. The droplet is initially making a  $\pi/2$  turn. A propagating steady state is eventually reached with a velocity of 7.41 m/s in the  $y$  direction, in very good agreement with the theoretical prediction  $V = 2U$  given in Eq. (17).

The important feature shared by all the simulations that we have seen in this section is the orientation of the droplets with respect to the direction of motion in the steady state. Specifically, in both Figs. 5(a) and 5(b), the droplet goes to steady-state motion only after it rotates in order to achieve the particular orientation. This is because the steady state achieved is a solitary wave; that is, the propagating droplet is a rigidly propagating solution of the Landau-Lifshitz equation. Such solutions have well-defined features. For example, the shape of the solitary wave defines its velocity. In our case, the particular orientation of the droplets gives a solitary wave velocity in the positive  $x$  axis for the case of Figs. 4 and 5(a) and in the positive  $y$  axis in the case of Fig. 5(b). Exchanging the positions of the skyrmion and the antiskyrmion would invert the direction (sign) of the velocity. One could conclude that the current sets the droplet in motion, revealing its solitary wave character.

Regarding the configuration of a traveling droplet, a heuristic argument can be given using the well-known dynamics of topological skyrmions. Under the current, the skyrmion Hall effect acts on the opposite topological charges of the two parts of the droplet. The skyrmion part is pushed to the one direction (upwards), while the antiskyrmion part is pushed to the opposite direction (downwards). This explains why the traveling droplet always acquires the same orientation.

In both Figs. 5(a) and 5(b), the droplet is deflected along the  $y$  axis during the initial stages of the motion. We do not have a full explanation of this phenomenon, but we give here a description of it. In the case of Fig. 5(a), the skyrmion Hall effect acting in the two parts of the droplet initially compresses it. Such a compressed droplet is expected to develop a velocity in the direction perpendicular to the line connecting its skyrmion and antiskyrmion parts. Since the droplet is rotated, the motion due to the compression is at an angle to the  $x$  axis, towards the positive  $y$  direction. The droplet is apparently again decompressed at approximately  $t = 60$  ns. After this time, the skyrmion Hall effect acts in the two parts to elongate the droplet. The rotating droplet is now deflected towards the negative  $y$  direction.

The solitary wave character of topologically trivial skyrmionic textures has been studied for the case of a skyrmionium, a topologically trivial,  $Q = 0$ , configuration in DM ferromagnets [11]. A static skyrmionium is axially symmetric, and a propagating one is elongated. A slowly moving skyrmionium presents Newtonian dynamics, and a fast moving one (velocity close to the maximum) presents relativistic dynamics [8].

## V. A DROPLET IN A DISK ELEMENT

Static chiral droplets are also found in the confined geometry of a magnetic disk-shaped element (a magnetic dot). We apply an energy relaxation algorithm as in Sec. III. This converges and gives a static skyrmion-antiskyrmion droplet for a wide range of parameter values.

We find droplets for a thickness  $d_f = 0.5$  nm and for similar parameter values as in the case of a film. In addition, we were also able to find stable droplets for larger thicknesses. Fig. 6 shows droplets in dots of two different sizes with  $d_f = 5$  nm and for different sets of parameter values. In

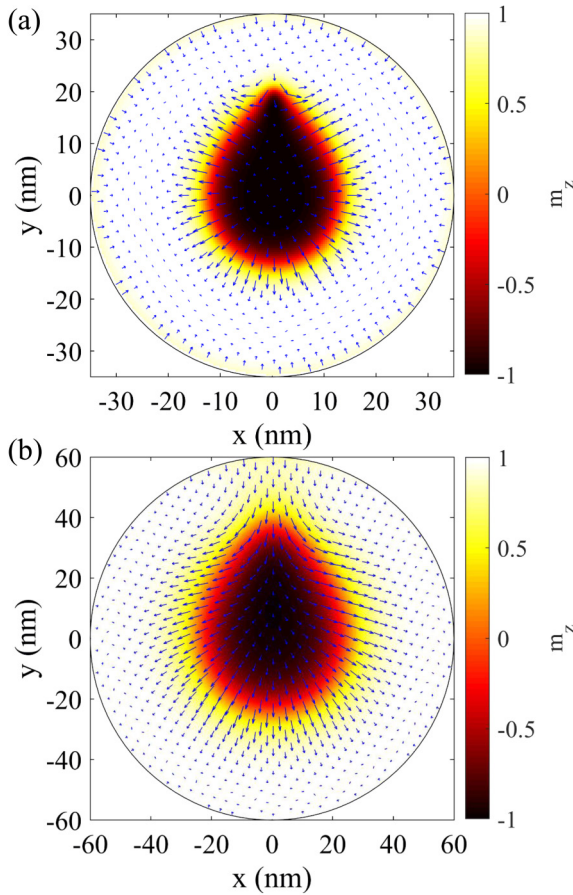


FIG. 6. Static skyrmion-antiskyrmion droplets in disk elements with thickness  $d_f = 5$  nm. (a) The disk diameter is  $d = 70$  nm. The parameter values are as in Table I. (b) The disk diameter is  $d = 120$  nm. The parameter values are  $D = 1$  mJ/m<sup>2</sup>,  $K = 4.43505 \times 10^5$  J/m<sup>3</sup> (other parameters are as in Table I). In this case, we have a more extended antiskyrmion part. For comparison, we note that a usual skyrmion (with  $Q = 1$ ) has an approximate radius of 15 nm for the dot in (a) and 30.5 nm for the dot in (b). They are thus somewhat larger than the corresponding  $Q = 0$  configurations shown here.

Fig. 6(a), we have a smaller dot, and the parameter values are the same as those used in Fig. 2 for the infinite film. The droplet is stable for a range of parameter values. For fixed  $\epsilon = 0.6086$ , the droplet is stable for  $3.0 \leq D \leq 7.6$  mJ/m<sup>2</sup> (when the anisotropy parameter  $K$  is appropriately varied).

In Fig. 6(b), we have a larger dot, and the parameter values (given in the caption) correspond to  $\epsilon = 3.16$  and  $\kappa = 0.00515$ . The value of  $\epsilon$  is outside the range for the existence of a skyrmion in a film (when the long-range part of the magnetostatic field is neglected). This shows that the effect of the magnetostatic field due to the confined geometry of a dot is substantial. The magnetostatic field from the lateral boundaries contributes to stabilizing the configuration. This phenomenon has already been noted in connection with magnetic bubbles in dots [29–31]. The effect is verified in the present case.

In the case of Fig. 6(b), the antiskyrmion part is smoother than in all other examples presented in this paper. This can be attributed to the magnetostatic field originating in the bulk in

combination with the DM interaction. It thus appears that the details of the configuration can be tuned, at least in the case of a droplet in a confined geometry.

In order to explore the origin of the configuration smoothing, we have calculated numerically droplets in a dot neglecting the magnetostatic field. We have observed that the droplet becomes smaller as the dot size decreases; thus, the boundaries do have an effect acting to shrink the droplet size (for the spin configuration at boundaries, see, e.g., Ref. [32]). However, we have not observed a smoothing of the droplet configuration. Therefore, the magnetostatic field is necessary to obtain a smoother droplet profile in a dot.

## VI. CONCLUDING REMARKS

We have found numerically skyrmionic textures that have both a skyrmion part and an antiskyrmion part (chiral droplets), with skyrmion number  $Q = 0$  in ferromagnets with perpendicular (easy-axis) anisotropy and DM interaction, including the magnetostatic field. They exist, in thin films, for a narrow range of parameter values. Under current, they move along the current exhibiting no Magnus force effect, and thus, their dynamics is different than the dynamics of  $Q = 1$  skyrmions. Their robustness is seen in their behavior under currents, where they persist for times long enough to fully reveal their dynamics.

In view of the predicted narrow range of parameters for their stability in infinite films, it would appear to be a challenge to observe them experimentally. Nevertheless, topologically trivial objects in the form of skyrmion-antiskyrmion pairs have already been observed [14]. Skyrmion-antiskyrmion pairs could also be very common as transient (short-lived) states. We expect that the results of the present paper will also help in understanding such states.

One could consider materials that support antiskyrmions, such as those reported in Ref. [7]. We have also found numerically skyrmion-antiskyrmion droplets in such systems. They are very similar to the droplets presented in this paper, except that the skyrmion part is replaced by an antiskyrmion part and vice versa. That is, the antiskyrmion part is larger, and the skyrmion part is smaller.

In materials with some special form of DM interaction, such as those studied in Ref. [6] (especially in Supplementary Note 1), the skyrmion and the antiskyrmion are both favored. In such models, a skyrmion-antiskyrmion droplet can be expected to have greater significance.

We have found that chiral droplets exist for a wider range of parameter values also in confined geometries. Given the robustness of the  $Q = 0$  droplets in magnetic dots, experimental observation of these appears to be plausible. Particular attention should be given to the dynamics of a  $Q = 0$  texture in a dot as it is expected to be different than the rotational dynamics of  $Q = 1$  skyrmions [33].

## ACKNOWLEDGMENTS

S.K. acknowledges funding from the Hellenic Foundation for Research and Innovation (HFRI) and the General Secretariat for Research and Technology (GSRT), under Grant No. 871. The authors thank the IIT Delhi HPC facility for



computational resources. We are grateful to the anonymous referees for indicating issues that have led to an expansion of this paper.

#### APPENDIX: STEREOGRAPHIC VARIABLE FOR SKYRMIONS

Skyrmion configurations often have a simple representation when we use the stereographic projection of the magnetization, defined as

$$\Omega = \frac{m_x + im_y}{1 + m_z}. \quad (\text{A1})$$

The axially symmetric form

$$\Omega_S = \frac{a}{\rho} e^{i\phi} = \frac{a}{x - iy}, \quad (\text{A2})$$

where  $(\rho, \phi)$  are polar coordinates and  $a$  is an arbitrary constant giving the skyrmion radius, represents a skyrmion of unit degree,  $Q = 1$ . The form

$$\Omega_A = \frac{a}{\rho} e^{-i\phi} = \frac{a}{x + iy} \quad (\text{A3})$$

has opposite winding than solution (A2), as seen in the sign of the complex exponent. Such a configuration has skyrmion number  $Q = -1$ , and it represents an *antiskyrmion*.

- 
- [1] K. Everschor-Sitte, J. Masell, R. M. Reeve, and M. Kläui, *J. Appl. Phys.* **124**, 240901 (2018).
- [2] A. P. Malozemoff and J. C. Slonczewski, *Magnetic Domain Walls in Bubble Materials* (Academic, New York, 1979).
- [3] A. N. Bogdanov and A. Hubert, *J. Magn. Magn. Mater.* **138**, 255 (1994).
- [4] S. Komineas, C. Melcher, and S. Venakides, *Nonlinearity* **33**, 3395 (2020).
- [5] A. N. Bogdanov and D. A. Yablonskii, *Sov. Phys. JETP* **68**, 101 (1989).
- [6] M. Hoffmann, B. Zimmermann, G. P. Müller, D. Schürhoff, N. S. Kiselev, C. Melcher, and S. Blügel, *Nat. Commun.* **8**, 308 (2017).
- [7] A. K. Nayak, V. Kumar, T. Ma, P. Werner, E. Pippel, R. Sahoo, F. Damay, U. K. Röbber, C. Felser, and S. S. P. Parkin, *Nature (London)* **548**, 561 (2017).
- [8] S. Komineas and N. Papanicolaou, *Phys. Rev. B* **92**, 064412 (2015).
- [9] N. Papanicolaou and T. N. Tomaras, *Nucl. Phys. B* **360**, 425 (1991).
- [10] S. Komineas and N. Papanicolaou, *Phys. D (Amsterdam, Neth.)* **99**, 81 (1996).
- [11] A. N. Bogdanov and A. Hubert, *J. Magn. Magn. Mater.* **195**, 182 (1999).
- [12] A. O. Leonov, U. K. Röbber, and M. Mostovoy, *EPJ Web Conf.* **75**, 05002 (2014).
- [13] W. Jiang, P. Upadhyaya, W. Zhang, G. Yu, M. B. Jungfleisch, F. Y. Fradin, J. E. Pearson, Y. Tserkovnyak, K. L. Wang, O. Heinonen, S. G. E. te Velthuis, and A. Hoffmann, *Science* **349**, 283 (2015).
- [14] J. Jena, B. Göbel, T. Ma, V. Kumar, R. Saha, I. Mertig, C. Felser, and S. S. P. Parkin, *Nat. Commun.* **11**, 1115 (2020).
- [15] L. Rózsa, K. Palotás, A. Deák, E. Simon, R. Yanes, L. Udvardi, L. Szunyogh, and U. Nowak, *Phys. Rev. B* **95**, 094423 (2017).
- [16] V. M. Kuchkin, B. Barton-Singer, F. N. Rybakov, S. Blügel, B. J. Schroers, and N. S. Kiselev, *Phys. Rev. B* **102**, 144422 (2020).
- [17] A. Vansteenkiste, J. Leliaert, M. Dvornik, M. Helsen, F. Garcia-Sanchez, and B. Van Waeyenberge, *AIP Adv.* **4**, 107133 (2014).
- [18] K. Palotás, L. Rózsa, E. Simon, L. Udvardi, and L. Szunyogh, *Phys. Rev. B* **96**, 024410 (2017).
- [19] L. Rózsa, M. Weißenhofer, and U. Nowak, *J. Phys.: Condens. Matter* **33**, 054001 (2020).
- [20] C. Moutafis, S. Komineas, and J. A. C. Bland, *Phys. Rev. B* **79**, 224429 (2009).
- [21] M. A. Hofer, T. J. Silva, and M. W. Keller, *Phys. Rev. B* **82**, 054432 (2010).
- [22] S. M. Mohseni, S. R. Sani, J. Persson, T. N. A. Nguyen, S. Chung, Y. Pogoryelov, P. K. Muduli, E. Iacocca, A. Eklund, R. K. Dumas, S. Bonetti, A. Deac, M. A. Hofer, and J. Åkerman, *Science* **339**, 1295 (2013).
- [23] N. R. Cooper, *Phys. Rev. Lett.* **80**, 4554 (1998).
- [24] S. Zhang and Z. Li, *Phys. Rev. Lett.* **93**, 127204 (2004).
- [25] A. A. Thiele, *Phys. Rev. Lett.* **30**, 230 (1973).
- [26] S. Komineas and N. Papanicolaou, *Phys. Rev. B* **92**, 174405 (2015).
- [27] K. Everschor, M. Garst, R. A. Duine, and A. Rosch, *Phys. Rev. B* **84**, 064401 (2011).
- [28] L. Döring and C. Melcher, *Calculus Var. Partial Differ. Equations* **56**, 60 (2017).
- [29] W. F. Druyvesteyn, R. Szymczak, and R. Wadas, *Phys. Status Solidi A* **9**, 343 (1972).
- [30] V. A. Ignatchenko and E. Y. Mironov, *J. Magn. Magn. Mater.* **124**, 315 (1993).
- [31] C. Moutafis, S. Komineas, C. A. F. Vaz, J. A. C. Bland, and P. Eames, *Phys. Rev. B* **74**, 214406 (2006).
- [32] S. Rohart and A. Thiaville, *Phys. Rev. B* **88**, 184422 (2013).
- [33] N. Sisodia, S. Komineas, and P. K. Muduli, *Phys. Rev. B* **99**, 184441 (2019).